

1 **TITLE PAGE**

2 **Image-based Cell Profiling Enables Quantitative Tissue Microscopy in Gastroenterology**

3 **Authors:**

4 \*John W. Wills<sup>1</sup>, Jack Robertson<sup>1</sup>, Huw D. Summers<sup>2</sup>, Michelle Minter<sup>1</sup>, Claire Barnes<sup>2</sup>, Rachel E.  
5 Hewitt<sup>1</sup>, Åsa V. Keita<sup>3</sup>, Johan D. Söderholm<sup>3</sup>, §Paul Rees<sup>2,4</sup>, §Jonathan J. Powell<sup>1</sup>.

6 § Contributed equally.

7

8 **Affiliations:**

9 <sup>1</sup>Biominerals Research, Cambridge University Department of Veterinary Medicine, School of  
10 Biological Sciences, Madingley Road, Cambridge CB3 0ES, UK.

11 <sup>2</sup>Centre for Nanohealth, Swansea University College of Engineering, Fabian Way, Crymlyn Burrows,  
12 Swansea SA1 8EN, UK.

13 <sup>3</sup>Department of Surgery and Department of Clinical and Experimental Medicine, Linköping  
14 University, 58193 Linköping, Sweden.

15 <sup>4</sup>Broad Institute of MIT and Harvard, 415 Main Street, Cambridge, MA 02142, USA.

16

17 **Running Headline:**

18 Image-Based Cell Profiling in Gastroenterology

19

20 **\*Corresponding Author Information:**

21 John W. Wills

22 Email: [jw2020@cam.ac.uk](mailto:jw2020@cam.ac.uk)

23 Tel: +447843 824042

24 <sup>1</sup>Biominerals Research, Cambridge University Department of Veterinary Medicine, School of  
25 Biological Sciences, Madingley Road, Cambridge CB3 0ES, UK.

26 **ABSTRACT**

27 Immunofluorescence microscopy is an essential tool for tissue-based research, yet data reporting is  
28 almost always qualitative. Quantification of images, at the per-cell level, enables ‘flow cytometry-  
29 type’ analyses with intact locational data but achieving this is complex. Gastrointestinal tissue, for  
30 example, is highly diverse: from mixed-cell epithelial layers through to discrete lymphoid patches.  
31 Moreover, different species (*e.g.*, rat, mouse and humans) and tissue preparations (paraffin /  
32 frozen) are all commonly studied. Here, using field-relevant examples, we develop open, user-  
33 friendly methodology that can encompass these variables to provide quantitative tissue microscopy  
34 for the field. Antibody-independent cell labelling approaches, compatible across preparation types  
35 and species, were optimised. Per-cell data were extracted from routine confocal micrographs, with  
36 semantic machine learning employed to tackle densely-packed lymphoid tissues. Data analysis was  
37 achieved by flow cytometry-type analyses alongside visualisation and statistical definition of cell  
38 locations, interactions and established microenvironments. First, quantification of *E. coli* passage  
39 into human small bowel tissue, following Ussing chamber incubations exemplified objective  
40 quantification of rare events in the context of lumen-tissue crosstalk. Secondly, in rat jejunum,  
41 precise histological context revealed distinct populations of intra-epithelial lymphocytes between  
42 and directly below enterocytes enabling quantification in context of total epithelial cell numbers.  
43 Finally, mouse mononuclear phagocyte – T cell interactions, cell expression and significant spatial  
44 cell congregations were mapped to shed light on cell-cell communication in lymphoid Peyer’s patch.  
45 Accessible, quantitative tissue microscopy provides a new window-of-insight to diverse questions in  
46 gastroenterology. It can also help combat some of the data reproducibility crisis associated with  
47 antibody technologies and over-reliance on qualitative microscopy.

48

49 **KEYWORDS**

50 Intestinal tissue, cell segmentation, machine learning, immunofluorescence, confocal microscopy,  
51 Processing tilescans in CellProfiler.

52

## 53 INTRODUCTION

54 Tissue microscopy provides powerful insights into biological processes across differing scales from  
55 sub-cellular to the macroscopic. For example, it enables distinct structural and sub-structural tissue  
56 regions to be defined as well as cell-cell spatial relationships to be observed (1-6). Indeed, *in situ*  
57 tissue-based research in gastroenterology is generally about scale, with compartment-specific  
58 analyses often desirable due to the specific physiology that occurs region-by-region. For example,  
59 cross talk between intestinal tissue and the luminal environment, cell differentiation along the crypt-  
60 villus axis and immune cell maps of gut lymphoid tissues are all active research areas which are, or  
61 could be, facilitated by quantitative, *in situ* measures (7-11).

62

63 In terms of *in situ* microscopy-based bioclinical research, immunofluorescence labelling and  
64 confocal imaging is the current mainstay, as it permits sensitive, quantifiable detection of multiple  
65 targets with subcellular localisation (12). Automated imaging has become standard, whilst new  
66 advances in artificial intelligence promise increased throughput through restoration of noisy images  
67 obtained at higher scan speeds (13). Yet, despite substantial advances in hardware and software,  
68 the majority of reported tissue microscopy 'data' remains qualitative and exemplified by the  
69 representative image. Typically, for tissue-based research, flow cytometry delivers the quantitative  
70 data and confocal microscopy is the visual means by which the spatial relationships and mechanics  
71 of biological processes are then conceptualised. There is, however, a clear advantage in combining  
72 these outputs to deliver quantification of cell types, their contents *and* their location, simultaneously.  
73 Indeed, the power of data mining from regular chromogen-based histology exemplifies such an  
74 approach even though the image data are lower resolution and less amenable to multi-label, per-  
75 cell quantification (4,5,12).

76

77 In fact, quantitative methodologies for the analysis of confocal microscope-derived tissue images  
78 have existed for at least fifteen years (1) and yet there remains a huge disconnect between what is  
79 possible and what has translated through to the biomedical community for everyday usage.  
80 Reasons for this have not been formally established, but interdisciplinary capability is a chief

81 suspect (14). Currently, joined-up approaches to deal with everything from optimal biological  
82 experimentation, through sample preparation and imaging, to the programming skills generally  
83 required for successful image analysis seldom reside under one roof within the biomedical  
84 community. There are also a number of philosophies as to what constitutes quantitative  
85 immunofluorescence microscopy, ranging from basic summation of fluorescence data across a  
86 given area, through integration within approximated cell-objects, to accurate per-cell identification  
87 and quantification (termed 'cell segmentation') (1,2,15). The latter has marked advantage as, within  
88 the limits of a microscope's resolution, it permits per-cell quantification of information in a manner  
89 amenable to familiar, flow cytometry-type gated analyses (1-3,16,17). It also allows distances to be  
90 established accurately, meaning that not only can cells be counted, but their content and spatial  
91 relationship to other cells or histological features can also be quantified (6).

92

93 Despite these advantages, accurate cell segmentation in tissues is complex, surprisingly sample-  
94 specific and time consuming for the non-expert (1,18). Much work to date has grown out of  
95 approaches established for cultured cells (19) as sample homogeneity facilitates image analysis.  
96 Generally, however, tissues are not at all homogenous. In the intestine, for example, a multi-cell  
97 epithelial layer with diffuse lymphoid tissue beneath (the lamina propria) may be juxtaposed to a  
98 dense B-cell dominant follicle with a different overlying epithelial layer (e.g., the Peyer's patch). For  
99 these reasons, accurate, quantitative, cell-based image analysis, compatible with such varying  
100 structure and delivered in a manner that is accessible to bio-clinical scientists has not yet been  
101 developed in gastroenterology.

102

103 Here, we demonstrate pragmatic methodology to enable per-cell immunofluorescence quantification  
104 from confocal microscopy-derived images of diverse gastrointestinal tissues, and we exemplify the  
105 approach with analyses of general interest to the field. We show how image-based cell profiling can  
106 take gastrointestinal tissue microscopy beyond representative images with quantification of (i)  
107 common or rare cellular events alongside (ii) their cell content and (iii) location, coupled with  
108 visualisation and statistical definition of cell-cell interactions and tissue microenvironments.

109 Importantly, we use open-source, user-friendly software platforms to carry out the work, and to  
110 construct quantitative pipelines, which similarly we provide here in open-access formats.

111

112

## 113 **MATERIALS & METHODS**

### 114 **ANIMAL TISSUE COLLECTION**

115 Mouse (9-12 week-old) and Rat (13 week old) tissues were collected from surplus healthy animals  
116 sacrificed for husbandry purposes by CO<sub>2</sub> asphyxiation and cervical dislocation. Ileal draining  
117 mesenteric lymph nodes were removed alongside jejunal / ileal intestinal samples (the latter  
118 containing Peyer's patches) in ~ 2 cm lengths. Upon excision, tissue samples were immediately  
119 plunge frozen into isopentane pre-cooled on melting dry ice, transferred to labeled cryovials, and  
120 stored in liquid nitrogen until use. Tissue samples for paraffin embedding were fixed in neutral  
121 buffered formalin ( $\geq 4$  h), before transfer to tissue cassette, and automatic processing by standard  
122 hospital protocol (dehydration by ethanol series, three changes of 100% xylene (at 30 °C), then  
123 three changes of paraffin wax (at 62 °C).

124

### 125 **HUMAN TISSUE COLLECTION & ETHICS**

126 Following informed consent and with approval from the Regional Ethical Review Board, Linköping,  
127 Sweden, specimens from the neo-terminal ileum next to the ileo-caecal valve were collected during  
128 surgery from one inflammatory bowel disease (IBD) patient with Crohn's disease (49 years, female)  
129 and one patient with colonic cancer (68 years, female), as a non-inflammatory bowel disease (non-  
130 IBD) control. The Crohn's disease patient had no anti-inflammatory medication and indication of  
131 surgery was ileitis. The tissue was macroscopically non-inflamed. The tissue from the colon cancer  
132 patient was free from cancer; the patient had no generalised disease and had not received  
133 preoperative chemo- or radiotherapy. Studies using human tissue were also approved by the UK  
134 NHS Health Research Authority, North West – Greater Manchester East Research Ethics  
135 Committee, REC reference 18/NW/0690.

136

137 **USSING CHAMBER EXPERIMENTS**

138 Human *ex vivo* tissue ileal samples were transported directly from the operating theater to the  
139 laboratory in Krebs buffer. Three tissue segments per individual were mounted in modified Ussing  
140 chambers (Harvard apparatus) as previously described (20). Transepithelial resistance and  
141 potential difference was used to assess tissue viability. Crohn's disease associated adherent  
142 invasive *Escherichia (E.) coli* strain LF82 were transformed with a plasmid (pEGFP, BD  
143 Biosciences) for expression of enhance green fluorescence protein (EGFP) as described previously  
144 (21). Live LF82 were then added to the mucosal side of the tissues at a final concentration of  $1 \times 10^8$   
145 CFU/mL. After 20 min, tissues were fixed in chambers with 4 % PBS-buffered paraformaldehyde for  
146 12 h at 4°C. The tissue samples were then immersed in 30% sucrose until embedded in optimal  
147 cutting temperature compound (OCT) for cryostat sectioning according to the protocol outlined  
148 below.

149

150 **TISSUE LABELLING & GENERAL IMMUNOFLUORESCENCE PROTOCOL**

151 For cryostat sectioning, frozen tissue samples were transported on ice and transferred into the  
152 cryostat chamber (- 20 °C) to acclimatise for 30 min. Samples were trimmed with a safety razor and  
153 transferred to moulds containing pre-chilled OCT (VWR, 00411243). Sections were cut at 12 micron  
154 thickness, picked up on superfrost plus coated slides (ThermoFisher, J1800AMNT) and rested at  
155 room temperature for at least 2 h prior to immunofluorescence labelling. Formalin fixed paraffin  
156 embedded (FFPE) sections were cut at 5 micron thickness, then fully dewaxed and rehydrated by  
157 baking at 60 °C for 1h, changing twice through xylene, a reverse ethanol series (100%, 70%, 50%,  
158 10%), followed by 1 min in water. All sections were then ringed with hydrophobic barrier pen (Vector  
159 Laboratories, H-4000) and unfixed cryostat sections were additionally fixed in 4% 0.1M phosphate  
160 buffered (pH 7.4) paraformaldehyde for 10 min. All sections were transferred to block buffer (10%  
161 goat serum (ThermoFisher, 16210064), 2% bovine serum albumin (Biosera, PM-T1726) diluted in  
162 25 mM Tris-buffered (pH 7.4) saline (TBS) containing 25 mM glycine) for at least 1 hour. The block  
163 buffer was removed, and 100 µL of the necessary primary antibodies in block buffer were added to  
164 each section (concentrations and manufacturer's codes specified, **Supplementary Table 1**).

165 Sections were incubated for 1 hour at room temperature under gentle agitation on a rocking  
166 platform. Each section was then washed thoroughly with three, 100  $\mu$ L changes of TBS. Nuclei were  
167 counterstained using a 1:2500 dilution of Hoechst 33342 (ThermoFisher, H3570) in TBS. Sections  
168 were washed once with 100  $\mu$ L TBS, prior to addition of the secondary antibodies (concentrations,  
169 manufacturer's codes and conjugated fluorophores shown in **Supplementary Table 1**). In with the  
170 secondary antibodies, phalloidin-AlexaFluor 647 (ThermoFisher, A22287) was included at  $\sim$  660 nM  
171 to label cell membranes in frozen sections, or, 20  $\mu$ g/mL wheat-germ agglutinin (WGA)-AlexaFluor  
172 647 (ThermoFisher, W32466) was used to label membranes in the FFPE sections. Secondary  
173 antibody and cell outlines stains were incubated with the tissue sections for 1 hour on a rocking  
174 platform. Each section was then washed with three changes of TBS prior drying carefully around  
175 each section with absorbent paper and mounting with #1.5 coverslips in Prolong Diamond mountant  
176 (ThermoFisher, P36965).

177

## 178 **GENERAL MICROSCOPY**

179 2-D images (typically 2048x2048 pixels per tile) were collected using sequential scanning on a  
180 Leica SP8 confocal microscope equipped with 405 nm, 488 nm, 562 nm and 633 nm lasers using  
181 plan-apochromat 63X/1.4 or 40X/1.3 oil immersion objectives. Tilescans were collected with 10%  
182 edge overlap using focus mapping to maximize throughput.

183

## 184 **IMMUNOFLUORESCENCE CONTROLS**

185 For each study, image data were obtained in a single run under identical settings, with supporting  
186 secondary-only, isotype and leave-one-out antibody controls included in tissue-matched serial  
187 sections to assess background fluorescence, non-specific binding and spectral cross-talk,  
188 respectively. For the Ussing's chamber work involving *E. coli* exposures to *ex-vivo* human tissues, a  
189 biological negative control (*i.e.*, images for tissue exposed to Krebs buffer alone without *E. coli*) was  
190 also included.

191

## 192 **TILESCAN PROCESSING CODE**

193 TileScans were stitched together using the 'Mosaic Merge' function in the Leica LASX software. The  
194 registered images were then cut up into ~ 4000x4000 pixel tiles with edge overlaps for processing  
195 with the open source and freely available CellProfiler (15) ([www.CellProfiler.org](http://www.CellProfiler.org)) software using a  
196 custom function called 'TileScanToCellProfiler'. This function structures the image data for input,  
197 and also stores user choices in a side-car information file for subsequent automated reassembly.  
198 After extracting per-cell data using CellProfiler, a second function called 'CellProfilerToTileScan' was  
199 written to reassemble the data. This reassembles the segmented cell masks (22) whilst removing  
200 'double-hits' on overlap edges. It also extracts and spatially reassembles all of the cell feature data,  
201 whilst assigning a unique, master cell identity number and the correct global cell position  
202 coordinates for every cell. These functions are provided for MATLAB and Python alongside example  
203 data and full instructions at the BioStudies database (<http://www.ebi.ac.uk/biostudies>) under  
204 accession number S-BSST305.

205

## 206 **SINGLE-CELL SEGMENTATION AND IMMUNOFLUORESCENCE QUANTIFICATION**

207 Cell segmentation results were obtained using CellProfiler and Ilastik (23) ([www.ilastik.org](http://www.ilastik.org))  
208 softwares. Example image data and analysis pipelines (built using CellProfiler version 3.1.9 and  
209 Ilastik 1.3.3) and accompanied by screen-cast video walkthroughs are available for download at the  
210 BioStudies database (<http://www.ebi.ac.uk/biostudies>) under accession number S-BSST305. Details  
211 of the section-type, species and tissue-type, objective lens and numerical aperture, image pixel  
212 density and the cell segmentation strategy used in every analysis are summarised in **Table S2**. In  
213 brief, villus mucosal tissues were segmented using a watershed approach, wherein nuclei were  
214 defined as primary objects before the actin (cryostat sections) or WGA (FFPE sections) delineated  
215 cell outlines were classified into cell-objects using a 'IdentifySecondaryObjects' module. As  
216 lymphoid tissues segmented poorly using the watershed approach, these images (*i.e.*, Peyer's  
217 patches, mesenteric lymph nodes (MLNs)) were first classified into 'cell outline', 'intracellular  
218 environment' or 'other / background' probability maps using pixel classification machine learning in  
219 the Ilastik software (feature selection shown, **Figure S1**, method exemplified, **Figure S2**). The  
220 resultant probability maps of each cell were then segmented to yield cell-objects via an



221 'IdentifyPrimaryObjects' module in CellProfiler. Immunofluorescence channels were preprocessed  
222 by two-class Otsu thresholding with a manual lower threshold set (independently for each analysis)  
223 at the level required to remove  $\geq \sim 95\%$  of fluorescence in tissue-matched, secondary antibody-only  
224 control images. Fluorescence intensity values per cell, alongside per-cell size and shape features  
225 were then measured for all channels by integration in each cell-object using the  
226 'MeasureObjectSizeShape' and 'MeasureObjectIntensity' modules in CellProfiler. In the same way,  
227 integration of thresholded images outputted as binaries was used to measure the fluorescence area  
228 per-cell. Cell features were written to both text files (*i.e.*, accessible via Excel spreadsheet), and  
229 MATLAB objects for subsequent analysis.

230

### 231 **SCORING SEGMENTATION ACCURACIES**

232 The pixel overlap agreement between manually and automatically segmented cell-objects was  
233 scored using the widely used intersection over union metric (Jaccard index) (24,25).

234

$$235 \quad J(P, G) = \frac{|P \cap G|}{|P \cup G|} = \frac{|P \cap G|}{|P| + |G| - |P \cap G|} \quad (1)$$

236

237

238 Where  $P$  and  $G$  are two sets containing pixel positions for the prediction ( $P$ ) and ground truth ( $G$ ),  
239 respectively. A score of 0 represents no overlap (*i.e.*, false negative) whereas 1 is a perfect, per-  
240 pixel overlap. With this approach, it is acknowledged that a value of  $\sim 0.7$  is a good segmentation  
241 result, and values of  $\sim 0.9$  lie close to human annotation accuracy (26). This benchmarking was  
242 carried out without first removing mis-segmented cells.

243

244

### 245 **SINGLE CELL DATA: PREPROCESSING**

246 To remove mis-segmented cells, plots of each cell-object's integrated nuclei and cell outline (*i.e.*,  
247 actin or WGA) scores were plotted according to data density using 'dscatter' (27). A cell population  
248 for analysis was then gated manually from these scatterplots using the inbuilt MATLAB function

249 'inpolygon' to trace the contour surrounding the main cell population. This selection was then held  
250 the same when processing all image-sets associated with an experiment (*i.e.*, experimental data  
251 and tissue matched controls).

252

## 253 **INTRAEPIHELIAL LYMPHOCYTES: IMAGE ANALYSIS**

254 Pixel classification machine learning in the Ilastik software was used to project masks for the  
255 epithelium, lamina propria and lumen 'tissue compartments' directly from the actin channel. In  
256 MATLAB, the epithelial mask was refined by filling isolated interior pixels using the inbuilt function  
257 'bwmorph', prior to performing an erosion followed by a dilation using disk structuring elements (5  
258 and 10 pixels, respectively) to bridge gaps. To find the different intraepithelial lymphocyte (IEL)  
259 subclasses, the resulting epithelial mask was skeletonised using 'bwskel', with spurs less than 500  
260 pixels removed. Expanding the skeleton using 'imdilate' with a disk-structuring element of 32 pixels  
261 then created a central path mask through each 'loop' of epithelium. The IEL sub-classifications  
262  $IEL^{sub}$  and  $IEL^{inter}$  were subsequently defined as  $CD3^+$  cells with centroids either inside the epithelial  
263 region, or inside this central path mask, respectively. The width of the central path was defined  
264 manually, by visually checking that  $IEL^{inter}$  events were consistently caught within the mask, whilst  
265  $IEL^{sub}$  events were excluded outside.

266

## 267 **STATISTICAL ANALYSES**

268 Non-parametric differences between data from different groups were analysed by Wilcoxon Rank  
269 Sum test. Statistically significant congregations of cells (*i.e.*, indicative of cellular zonation) were  
270 identified relative to what would be expected by random chance given the frequencies of different  
271 cell types present using the Getis-Ord  $G_i^*$  statistical approach (28). This measures the spatial  
272 concentration of values  $x_j$  associated with  $j$  values within a distance  $d$  of the value  $x_i$ . The ratio  $G$  is  
273 defined as:

274

$$275 \quad G_i(d) = \frac{\sum_{j=1}^n w_{ij}(d)x_j}{\sum_{j=1}^n x_j} \quad (2)$$

276

277 where  $w_{ij}(d)$  defines the contribution to the numerator of the ratio depending on the distance  $d$ , for  
278 example using *i.e.*,  $w_{ij}(d) = 1$  if  $d_{ij} < d$  else;  $w_{ij}(d) = 0$  if  $d_{ij} > d$ . The Getis-Ord statistic is then given  
279 by:

$$280$$
$$281 \quad Z[G_i(d)] = \frac{[G_i(d) - E(G_i(d))]}{\sqrt{\text{var } G_i(d)}} \quad (3)$$

282

283 Where,  $E(G_i(d))$  represents the expected fraction of items within  $d$ , assuming a completely random  
284 distribution calculated as:

$$285$$
$$286 \quad E(G_i(d)) = \frac{\sum_j \omega_{ij}(d)}{n-1} \quad (4)$$

287

288 The value  $Z[G_i(d)]$  now describes the difference in the fraction of values within the distance  $d$  from  
289 location  $i$  from the random expected value relative to the standard deviation. In our example we  
290 discretise the field of view into a grid and value  $x_i$  is defined as the number of cells of a certain  
291 phenotype in the grid position  $i$ .

292

293

## 294 **RESULTS**

295 With a specific focus on intestinal tissues, this work aims to develop and demonstrate open, user-  
296 friendly methodologies that enable per-cell immunofluorescence quantification *in situ* using routine,  
297 confocal microscopy-derived images. Here, we focus on analysis of 2-D images, as qualitative  
298 display in this format is the current standard in the bio-clinical sciences.

299

### 300 **Labelling Gastrointestinal Tissues for Cell Segmentation**

301 First, we sought simple fluorescence labelling strategies compatible across species (*i.e.*, antibody  
302 independent) for the purpose of delineating individual nuclei and cell outlines for subsequent cell  
303 segmentation. For both human and murine ileal sections, cut from either regular paraffin-embedded

304 (*i.e.*, FFPE) or snap-frozen and OCT embedded tissues, the fluorescent nuclear dye, Hoechst  
305 33342, provided a straightforward, reliable means to label cell nuclei (**Figure 1A-L**). Different  
306 strategies were required however to clearly delineate cell outlines in the two different section-types.  
307 Frozen sections exhibited artefacts when cell membranes were directly labelled using phospholipid  
308 labelling with wheat germ agglutinin (WGA) conjugates. This was especially notable at goblet cell  
309 sites, and is likely explained by non-specific binding to mucins (**Figure S3**). To avoid this, actin  
310 cytoskeletal staining via fluorescent phalloidin conjugates was used, and provided good  
311 demarcation of cell outlines (**Figure 1A-D**). In contrast, for FFPE sections the situation was  
312 reversed. The cell actin filaments labelled by phalloidin conjugates were destroyed by alcohol  
313 exposure during the formalin fixation process and thus could not be labelled for cell outline  
314 determination (**Figure S3**). However, in FFPE sections, direct cell membrane labelling with WGA  
315 was a successful strategy (**Figure 1E-H**) probably because mucins were cleared when exposed to  
316 the solvents during processing.

317

### 318 **Cell Segmentation Strategies Using Open Source Tools**

319 With approaches for per-cell labelling established, we next considered cell segmentation strategies.  
320 Once again, dual strategies were necessary but, this time, dependent upon tissue region rather than  
321 tissue processing. For villus regions where cells are not tightly packed but cell types vary greatly in  
322 shape, and cell outlines are not always clear, a routine seeded watershed approach, readily  
323 deployed in CellProfiler appeared best. With this, the nucleus of each cell is first segmented and  
324 then used as an anchor point from which to define each cell's outline (**Figure 1A-D**). In densely  
325 packed, pure lymphoid tissue (*e.g.*, MLN or Peyer's patch), however, there were difficulties in  
326 accurately resolving individual nuclei and the resulting watershed approach performed poorly  
327 (**Figure S4**). To resolve this, pixel classification machine learning in the Ilastik software was used to  
328 convert these images into probability maps of 'cell outlines', 'intracellular environments' or  
329 'background / other' (shown, **Figure S2**). The intracellular probability map was then directly  
330 segmented into cell objects in CellProfiler using a IdentifyPrimaryObjects module (**Figure 1E-L**). Of  
331 note, this latter approach (i) only required cell outline information (*i.e.*, actin or WGA) for effective

332 segmentation, freeing up the nuclear channel for other targets and (ii) was compatible with lower-  
333 resolution input images (e.g., **Figure 1I-L**), as results depend not upon contrast boundaries in the  
334 source image but upon derived probability maps. Thus, in conjunction with the antibody-  
335 independent, tissue labelling strategies outlined above, these strategies permit cell segmentation  
336 across diverse intestinal tissues and are readily transferable between species and section-types  
337 (e.g., mouse, rat, human; villus mucosa, Peyer's patch, MLN; frozen and paraffin embedded are  
338 demonstrated, **Figure 1**). For all analyses, histological information alongside imaging specifics and  
339 the cell segmentation strategy used are summarised in **Table S2**.

340

### 341 **Accuracy of Cell Segmentation**

342 The automated cell segmentations presented in **Figure 1**, which are derived across varying species  
343 and tissue preparations, were benchmarked – cell-by-cell – against hand-drawn manual  
344 segmentations using the commonly employed intersection over union approach (Jaccard index) (24-  
345 26) (>1000 cells scored; **Figure S5**). This benchmarking was carried out without first removing mis-  
346 segmented cells. Median scores in terms of pixel overlap were consistently between 0.80 – 0.83,  
347 with scores of ~ 0.9 recognised as the maximum realistically feasible with this approach due to the  
348 inherent accuracy limits of the manual segmentation itself (*i.e.*, due to line thickness, outline  
349 smoothing *etc.*), and 0.8-0.9 considered strong agreement (26) (exemplified, **Figure S5**).

350

### 351 **Open Source Image Analysis**

352 The source images and the complete CellProfiler / Ilastik image analysis pipelines, which are  
353 necessary to enable the segmentation strategies shown in **Figure 1**, are provided at the BioStudies  
354 database (<http://www.ebi.ac.uk/biostudies>) under accession number S-BSST305. Both the  
355 CellProfiler and Ilastik softwares are freely available, and no programming is required for  
356 implementation of the image analysis routines described. Results, for example per-cell shape and  
357 immunofluorescence quantifications can be outputted as text files easily openable as EXCEL  
358 sheets, or saved as MATLAB or HDF5 objects.

359

## 360 Immunofluorescence Quantification and Exclusion of Debris

361 Following cell segmentation, per-cell immunofluorescence quantification was implemented by  
362 CellProfiler pipeline using Otsu thresholding and the 'MeasureObjectIntensity' and  
363 'MeasureObjectSizeShape' modules – as described in the Methods. Here, we subsequently chose  
364 to process the outputted tables of per-cell measurements using MATLAB. One aspect in tissues that  
365 required a different approach from *in vitro* cells was the determination of mis-segmented cell-objects  
366 that should be discarded prior to analysis (*i.e.*, the debris equivalent of flow cytometry). For cultured  
367 cells, a recommended approach involves discarding objects that lie outside of the 5% or 95%  
368 percentiles by size (19). In tissue however, this approach is less effective due to the diversity of  
369 cross sectional cell shapes and sizes including the occurrence of infrequent cell types of irregular  
370 size. Instead, simple density plots (*e.g.*, insets, **Figure 1 B/F/J**) of each cell-object's integrated  
371 nuclear and cell outline fluorescence (*i.e.*, WGA or actin) provided a route to gate out poorly  
372 segmented cells. Events that fell outside of the main population due to abnormally high (*e.g.*,  
373 doublets) or low (*e.g.*, true debris) signals were excluded (discarded events exemplified, **Figure 1 -**  
374 grey squares). A further advantage of this approach is that cells just partially clipped by the optical  
375 section tend to get removed, providing more consistent sampling of cells' cross-sectional  
376 immunofluorescence data.

377

## 378 Rare Events: *E. coli* Passage into Ileal Tissue

379 To demonstrate how image-based cell profiling can tackle rare event analysis of intestinal tissue,  
380 the passage of GFP-labelled *E. coli* strain LF82 into human ileum was considered (**Figure 2**). Three  
381 tissue samples taken from one non-IBD patient with colon cancer, and one IBD patient with  
382 macroscopically non-inflamed Crohn's disease, were investigated. A fourth tissue sample from the  
383 Crohn's patient was exposed to Krebs buffer alone (*i.e.*, without *E. coli*) as a biological negative  
384 immunofluorescence control (**Figure 2A-C**).

385

386 Images were collected from villus tissue regions across ~ 6-8 tissue sections taken at random  
387 intervals throughout each biopsy. This approach enabled rapid sampling from across the full

388 dimensions of each tissue sample. As expected, no punctate spots of anti-GFP fluorescence were  
389 observed in the tissue biopsies exposed to Krebs buffer only (**Figure 2A**). In each of the three  
390 cancer control non-IBD tissue biopsies, the few *E. coli* that were observed were bound to the apical  
391 side of the epithelium (indicated, **Figure 2B**). Contrastingly, in all three tissue biopsies from the  
392 patient with Crohn's disease, transmucosal *E. coli* were identified within both the epithelial layer and  
393 lamina propria (**Figure 2C**).

394

395 The aim of this work, however, was to move beyond careful qualitative observation – as described  
396 above – to objective *quantification*. To this end, the watershed approach developed for mucosal  
397 tissue rapidly allowed per-cell assessment of ~ 5,000 cells per tissue sample. The background  
398 fluorescence distribution was then established on the tissue sample exposed to Krebs buffer alone  
399 by plotting a cell-number normalised histogram of the signal in the anti-GFP channel (total cells  
400 analysed = 5,475). When this step was repeated for the non-IBD tissue samples that had been  
401 exposed to *E. coli*, virtually no signal – above the established background – was observed (**Figure**  
402 **2D**, 14,671 cells analysed). This demonstrated that the *E. coli* were not readily able to achieve  
403 transmucosal passage within the exposure timeframe in the non-IBD tissues. In contrast, when this  
404 was repeated in the Crohn's disease tissue samples, a positive increase in the per-cell fluorescence  
405 distribution was observed (**Figure 2D**, 15,226 cells analysed). Comparison of this increase relative  
406 to the non-IBD group showed significance at the  $p < 0.001$  level (Wilcoxon rank sum, **Figure 2E**).

407

408 Oftentimes it is convenient to call a cell as simply 'positive' or 'negative' – in this case meaning cells  
409 with anti-GFP fluorescence indicative of  $\geq 1$  *E. coli* event or none. As with flow cytometry, gating is  
410 required to determine this cut off and, again as for flow cytometry, there is a degree of subjectivity  
411 relating to the stringency of specificity versus sensitivity. Here, when a gate was applied above the  
412 defined background fluorescence (indicated in **Figure 2D**), then the number of anti-GFP positive  
413 cells in the Crohn's disease tissue was just 282 or 1.85%. The data therefore demonstrate how the  
414 image-based cell profiling approach can quantify rare events objectively, substantiating the  
415 representative images shown.

416

### 417 **Processing Large Unbroken Image-Fields: Working With Tilescans**

418 Working with sets of individual images, obtained randomly across multiple tissue sections, as  
419 above, is one approach in image-based cell profiling. However, under other circumstances it may be  
420 desirable to work with high resolution, unbroken fields (*i.e.*, tilescans) in which per-cell  
421 immunofluorescence analyses can be augmented by histological context (tissue mapping).  
422 CellProfiler does not currently possess dedicated modules for processing tilescans, and it is often  
423 not possible to directly process input images much larger than ~ 4,000 x 4,000 pixels due to  
424 memory limitations on the local machine. For this reason, here we developed two software functions  
425 specifically aimed at processing immunofluorescence tilescans. The first, which we call  
426 'TilscanToCellProfiler', takes stitched tilescans directly in most proprietary microscopy formats and  
427 cuts them into a series of user-defined, manageably-sized tiles for CellProfiler input. After  
428 processing, a second function called 'CellProfilerToTilscan' seamlessly reassembles the cell  
429 segmentation and spatial positions of the extracted, per-cell data. These functions can be deployed  
430 with a single line of code in the programming environments MATLAB or Python. Example images,  
431 code and full instructions for the non-expert are provided at the BioStudies database  
432 (<http://www.ebi.ac.uk/biostudies>) under accession number S-BSST305.

433

### 434 **Machine-Learning Tissue Compartments: The Intestinal Epithelium**

435 The highly convoluted shape of the gastrointestinal mucosa makes accurate, region-of-interest  
436 selections for different tissue 'compartments' (*e.g.*, epithelium, lamina propria, *etc.*) complicated  
437 and time consuming to perform. At the same time, compartment-specific analyses are often  
438 desirable due to the specific physiology that occurs region-by-region. To demonstrate the  
439 automation of compartment-specific gastrointestinal analysis, we set out to profile intra-epithelial T  
440 lymphocytes in longitudinal frozen sections of rat jejunum – just using a single CD marker and the  
441 histological context afforded by *in situ* microscopy. To accurately identify the epithelium, one of a  
442 pair of serial frozen sections was immunolabelled for epithelial cell adhesion molecule (EPCAM) –  
443 alongside nuclei and actin. This precisely pinpointed the location of the epithelial region between the



444 basement membrane and the apical enterocyte surface (29-31) (**Figure 3A**). Using this EPCAM  
445 labelling as a guide to inform pixel annotation, we then trained an Ilastik machine learning model to  
446 mask the epithelium, as well as the lumen and lamina propria tissue compartments, *directly* from the  
447 actin channel itself. In this way, the EPCAM labelling was no longer required (**Figure 3B**) (process  
448 exemplified stepwise, **Figure S6**). Of note, we also found that the same approach worked with WGA  
449 labelling in FFPE sections (demonstrated, **Figure S6E**).

450

### 451 **Utilising Locational and Cellular Information: Profiling Intraepithelial Lymphocytes**

452 Next, we set out to utilise both tissue compartment and per-cell image-data to profile intraepithelial  
453 T lymphocytes in the jejunal mucosa. In the second serial section, a 112-image tilescan containing a  
454 wide region of villous mucosa was collected with anti-CD3 labelling to identify T cells. As both the  
455 EPCAM and CD3 antibodies were raised in the same host, instead of dual-labelling, the tissue  
456 compartment model was deployed in the mucosa to provide a mask for the epithelium (**Figure 3C**).

457

458 To understand and quantify background fluorescence, as well as the non-specific binding capacity  
459 of the CD3 antibody in the rat jejunal tissue, set of ten image-fields for either the secondary-  
460 antibody alone (*i.e.*, 2<sup>o</sup> only control), or the secondary plus an irrelevant primary antibody of the  
461 same isotype (*i.e.*, an isotype control) were collected for the CD3 channel in adjacent, serial  
462 sections. Per-cell immunofluorescence data was then extracted from the CD3 tilescan (~ 60,000  
463 cells) and control image-sets (~ 6,000 cells) using the watershed cell segmentation pipeline  
464 optimised for mucosal tissue (above). A CD3<sup>+</sup> cell population was then formed by gating cells with  
465 per-cell fluorescence values greater than those observed in the 2<sup>o</sup>-only and isotype controls (*i.e.*, as  
466 is typical in flow cytometry) (**Figure 3D**). Cell centroid markers were displayed on each gated cell, to  
467 help pinpoint CD3<sup>+</sup> T lymphocytes both visually and for subsequent locational categorisation..  
468 Interfacing this gated cell population with the epithelial mask allowed further division of the CD3<sup>+</sup> cell  
469 population into intra-epithelial lymphocyte (IEL) and lamina propria T cell subpopulations by  
470 identification of cells with centroids inside or outside of the mask (**Figure 3D**). Upon close study of  
471 the defined IEL CD3<sup>+</sup> cells in context of the masked epithelium, it was clear that this cell population

472 existed in two distinct forms. IEL events were either observed in close association with the basal  
473 aspect of enterocytes (hereafter termed 'IEL<sup>sub</sup>'), or, were *truly* between individual enterocytes  
474 (hereafter termed 'IEL<sup>inter</sup>'). To split the IELs into these two classes, the epithelial mask was  
475 subjected to a morphological process called skeletonisation. This reduced the epithelial mask to  
476 yield a central path through each 'loop' of villus epithelium (process exemplified, **Figure S6**).  
477 Inclusion within this sub-mask allowed the central, IEL<sup>inter</sup> population to be separated out, leaving  
478 behind the IEL<sup>sub</sup> cells (**Figure 4A-E**).

479

480 In this way, harnessing per-cell fluorescence data in combination with the precise histological  
481 context provided by the high-resolution tilescan allowed the identified CD3<sup>+</sup> cells to be subdivided  
482 into three distinct subpopulations (*i.e.*, lamina propria CD3<sup>+</sup> (LP<sup>CD3+</sup>), IEL<sup>sub</sup> and IEL<sup>inter</sup>). This,  
483 alongside the segmentation of all cells, whether immunolabelled or not, provided data well suited to  
484 automated cell counting in the context of a tissue map. Hence, we measured the areas occupied by  
485 the different designated compartments – alongside their cell counts – in total, per 100 cells, and as  
486 ratios between the different tissue compartments (**Figure 4F-I**). Interestingly, whilst not so apparent  
487 visually, the epithelium occupied a greater area (**Figure 4F**) and contained more total cells (**Figure**  
488 **4G/I**) than the underlying lamina propria. CD3<sup>+</sup> cells were also determined more abundant per-cell  
489 in the lamina propria than in the epithelium (**Figure 4I**). Meanwhile, whereas IELs were quite  
490 common, the IEL<sup>inter</sup> sub-class were rare events (~ 4 per 100 epithelial cells). This was especially  
491 true when compared to the IEL<sup>sub</sup> class, at ~ 13 per 100 epithelial cells (**Figure 4H/I**).

492

### 493 **Cell Interactions and Expression: Mapping in the Peyer's Patch**

494 Access to per-cell immunofluorescence data collected *in situ* provides the opportunity to consider  
495 both cell expression and physical cellular interactions via nearest-cell neighbour analyses.

496 Lymphoid tissues represent one such environment in which interaction and expression data are of  
497 key importance. Here we considered CD11c<sup>+</sup> mononuclear phagocyte – CD3<sup>+</sup> T cell expression  
498 and interactions in a transverse section of mouse Peyer's patch (24 image tilescan, ~ 16,000 cells)

499 **(Figure 5)**. A basic overview of the structure and cellular zonation of the murine Peyer's patch is  
500 provided in **Figure S7**.

501

502 Image-data were collected for six channels: fluorescence data were collected for nuclei, actin,  
503 CD11c (for mononuclear phagocytes; *i.e.*, antigen presenting cells) and CD3 as a pan T-lymphocyte  
504 marker. Alongside, transmitted and reflected light were also collected to inform on overall histology  
505 and section quality (**Figure 5A**). As before, data for the respective 2<sup>o</sup>-only and isotype controls were  
506 also collected alongside in tissue-matched serial sections. As per-cell immunofluorescence  
507 quantification was to be carried out on two of the channels (*i.e.*, CD3 and CD11c), leave-one-out  
508 control image-sets were also taken to check for any fluorescence cross-talk between channels. This  
509 involved labelling additional serial sections with either CD11c or CD3, yet collecting the respective  
510 fluorescence data for both channels. In this way, any cross-talk into the 'empty' channel could be  
511 detected in the resultant per-cell fluorescence distributions.

512

513 Using the Ilastik / CellProfiler machine learning cell segmentation pipeline, alongside the software  
514 reassembly (tilescan) functions described above, the lymphoid tissue was segmented seamlessly  
515 across the entire Peyer's patch (**Figure 5B**). A region-of-interest (ROI) was then set around the  
516 lymphoid tissue, and just the CD11c and CD3 immunofluorescence data were shown on top of the  
517 segmented-cell outlines inside the ROI. Outside of the ROI, just the actin staining was displayed, to  
518 provide histological context (**Figure 5C/D**). This visualisation approach was found to dramatically  
519 reduce the visual complexity of the six-channel image, permitting display of most important  
520 information in a per-cell and visually intuitive manner – across the scale of the entire lymphoid  
521 follicle.

522

523 To build CD3<sup>+</sup> and CD11c<sup>+</sup> cell populations, after debris removal (discussed above), gating was first  
524 used to select cells with fluorescence values above those observed in the 2<sup>o</sup>-only and 'leave-one-  
525 out' controls. The fluorescence distributions of the isotype controls were also used to inform gating.  
526 Here, whilst we gated above values high enough to remove > ~ 99% of cells from the isotype

527 distributions, gating at the maximum was avoided for fear of building highly specific, yet poorly  
528 sensitive cell populations (**Figure 5E**). Due to the closely packed cells, and in conjunction with the  
529 expression of CD11c and CD3 immunofluorescence on the cell membrane, it was found that adding  
530 a second sequential gate on the area of fluorescence within each cell helped to reduce 'bystander-  
531 positive' events caused by small amounts of fluorescence spanning the segmented-cell outlines and  
532 manifesting in immediately adjacent neighbouring cells (further discussion/exemplification provided,  
533 **Figure S8**). In this way, cells exhibiting CD marker fluorescence all around their perimeters were  
534 better isolated from their immediate neighbours, whilst maintaining sensitivity (**Figure 5F, inset**). To  
535 aid this second gating step, cell-centroid markers for the identified cell populations were placed onto  
536 the immunofluorescence images, as described above, providing visual feedback (**Figure 5F**). As  
537 expected, the sub-epithelial dome (SED) was rich in mononuclear phagocytes and the inter-follicular  
538 region (IFR) at the right of the image contained large numbers of T-cells. Surprisingly however, a  
539 population of highly juxtaposed, CD11c-CD3 neighbouring cells (*i.e.*, region shown in **Figure 5D**)  
540 that *still* identified positive in both gates after bystander removal were identified, indicating an  
541 interaction (17) relative to other cells, and suggesting a likelihood of cell-cell communication (**Figure**  
542 **5F**).

543  
544 In addition to placing markers on cell centroids to delineate the gated cell populations (**Figure 6A**),  
545 other methods capable of clearly visualising the single-cell data and consequent spatial  
546 relationships across the scale of the complete Peyer's Patch were sought. In **Figure 6B**, the  
547 marker-placement view was simplified further by flood-filling the individual segmented cell masks to  
548 clearly show the populations in a manner that could be effectively visualised at small size. The  
549 absence of immunofluorescence labelling (*i.e.*, black, CD11c<sup>-</sup> / CD3<sup>-</sup> regions) was also informative,  
550 as within the patch, the vast majority of these double-negative cells will be B lymphocytes (32).  
551 Next, the flood-filled view was simplified further to only show CD11c cells with touching CD3  
552 nearest-cell neighbours (including juxtaposed CD11c/CD3 cells) (**Figure 6C**). In this way, the view  
553 gives a sense of the spatial distribution of APCs within interactive distances of T lymphocytes.  
554 Interestingly, it was observed that the majority of these events were predominantly congregated

555 around B cell follicles in the germinal center (GC) region, and were much less apparent in the SED  
556 where, probably, MNP – B cell interactions may predominate (33).

557

558 Having successfully identified populations of cells, next we moved forwards to consider  
559 quantification of per-cell fluorescence (*i.e.*, related to protein expression). To do this, we made use  
560 of the ~ 800 nm optical Z plane afforded by the confocal optics and high numerical aperture  
561 objective (63X/1.4) to isolate a thin plane through *individual* cells. The analysis was also aided by  
562 the ability to select for cell objects optimally cross-sectioned through their central plane during the  
563 debris removal step (discussed above), as this improved measurement consistency by sampling  
564 data from similar, central regions in each cell. To clearly visualise the data from across the whole  
565 lymphoid follicle within a reasonable figure-size, the per-cell expression of CD11c and CD3 was  
566 displayed in four intensity bands (*i.e.*, dim, low, intermediate and high) (**Figure 6D/E**). Perhaps  
567 unsurprisingly given the highly mixed population of mononuclear phagocytes delineated by CD11c,  
568 no clear spatial patterning according to CD11c expression was observed (**Figure 6D**). For CD3  
569 however, the IFR at the right of the patch, in addition to the APC and T-cell zones around the GC  
570 were rich in CD3<sup>int/hi</sup> events, whilst the marginal zone and SED were predominated by CD3<sup>dim/lo</sup>.  
571 This may be related to T cell sub-types, or activation, and deserves further scrutiny (34).

572

573 Finally, we also sought a method to statistically identify significant spatial congregations of cells so  
574 that regions of cellular zonation / established cellular microenvironments could be defined across  
575 the lymphoid follicle. To do this we harnessed both the cell location and CD11c or CD3 per-cell  
576 expression data and used these to calculate the Getis-Ord GI\* spatial statistic (28). This provided a  
577 heat map identifying where statistically significant, spatial congregations of different cell types  
578 occurred relative to what should be expected by random chance – given the frequencies of the  
579 different cell types involved (**Figure 6F**). As expected, the SED was significantly rich for CD11c, as  
580 was the IFR for CD3. For both cell types however, the maps also revealed a wealth of complex  
581 microstructure surrounding B-cell follicles in the GC. Under the ‘steady state’ normal biology

582 depicted here, it was also noted that the SED was sparse in terms of congregating CD3<sup>+</sup> T-  
583 lymphocytes.

584

## 585 **DISCUSSION**

586 Here, with a specific focus on intestinal tissues, we develop open, user-friendly methodology that  
587 enables per-cell quantification using routine confocal micrographs. As a methodological  
588 advancement, it is important that the findings here are seen as a range of examples around  
589 capability, rather than individually-powered biological studies. Notwithstanding, we flag areas where  
590 the technique revealed interesting findings, including measures of spatially distinct IEL sub-  
591 populations – being either between or beneath enterocytes in the villus mucosa – and the complex  
592 microstructure of cellular zonation in the Peyer's patch, including spatial distributions of APC-T cell  
593 interactions.

594

595 Our image-based cell profiling approach delivers data in three key ways: (i) it enumerates different  
596 cell types, as in flow cytometry, but it also (ii) provides precise cellular locational data with  
597 histological context and (iii) resolution and quantification of cell contents. To achieve this, a number  
598 of novel approaches had to be developed or bridged together. Firstly, we provide routes in MATLAB  
599 or Python to enable tilescan processing with CellProfiler – to include spatial reassembly of the  
600 mined per-cell data and the production of global segmentation masks with unique cell identities to  
601 enable visualisations. Secondly, to permit accurate cell segmentation, antibody-independent cell  
602 labelling was employed, which we optimised for both FFPE and frozen intestinal tissue sections.  
603 Importantly this approach does not use up antibody hosts and transfers easily and directly between  
604 species. Next, effective per-cell immunofluorescence analysis requires accurately segmented cells  
605 with mis-segmented cells (debris) excluded. We show how this can be achieved using density plots  
606 to refine a consistently sampled cell population, with the outliers (partial cells or doublets) excluded.  
607 Alongside, to tackle the difficult issue of dense cell packing in lymphoid tissues, we use semantic  
608 machine learning within a fast, user-friendly framework (23) to yield accurate cell segmentations.  
609 Finally, we demonstrate how inadvertent bystander-positive cells can be obviated through

610 sequentially gating on fluorescence intensity followed by fluorescence area, and suggest that any  
611 remaining bystanders are indicative of cell-cell interactions. We also demonstrate how spatial  
612 statistics can be employed to better define tissue microenvironments in terms of identifying  
613 significant cellular congregations.

614

615 Here we use the popular CellProfiler software as a 'backbone' to enable per-cell quantification.  
616 Importantly, its pipeline-based style is extremely flexible, and can use original, deconvolved and / or  
617 spectrally unmixed input images from almost any microscope or upstream software package.  
618 Moreover, the pipelines provided here can also utilise probability maps to enable cell segmentation  
619 from any source, including, where necessary, more advance machine learning approaches such as  
620 deep convolutional neural networks (26). Of note, a delivery of the increasingly popular Unet  
621 architecture within the user-friendly environment of Ilastik is planned for release in spring 2020 (35).

622

623 In embracing such a technical approach to tissue analysis, it is critical that the fundamentals of robust  
624 immunofluorescence methodology are not overlooked. In our experience, best possible tissue  
625 orientation helps greatly in interpretation of outputs. Moreover, our approach does not obviate good  
626 practice in labelling and imaging: rather, success relies upon it. Controls, to assess background  
627 autofluorescence and non-specific antibody binding, are extremely important, alongside assurance  
628 that fluorescence signals do not cross between channels. Here, we have demonstrated the use of  
629 2°-only, isotype, leave-one-out and biological negative controls collected in tissue-matched, serial  
630 sections to assess these parameters. We then use Otsu thresholding in conjunction with gated  
631 analyses to accurately isolate cell populations and measure cell expression / contents. Of course,  
632 these controls in themselves do not ensure that the correct target is being labelled and, as always in  
633 such work, proper validation of antibodies remains essential (36,37).

634

635 Our accessible approach to per-cell analysis of tissue sections contrasts with other techniques.  
636 Whilst imaging mass cytometry (*e.g.*, 'CyTOF'), enables the use of dozens of antibody markers, it  
637 has lower spatial resolution and necessitates highly specialist instrumentation for detection (6,18).

638 Although high throughput and extremely powerful within diagnostic pathology, packages that permit  
639 the analysis of chromogen stained slide-scans lack the resolution, sensitivity, ability to multiplex and  
640 quantitate immunolabelled targets in a way that is often required for precision research (12).  
641 Meanwhile, commercial 'all-in-one' solutions, such as those employing fluorescence slide scanners  
642 or spinning disk confocal techniques, are (i) expensive, especially when highly capable confocal  
643 microscopes are already available at most research institutions and (ii) rely on software with the  
644 unenviable task of enabling the analysis of all conceivable tissue types. In our experience, this  
645 results in approximate per-cell measurements. In contrast, focussing in one field and interfacing  
646 different strategies (18), as we do here with the intestine, enables precision cell segmentation to be  
647 achieved and thus accurate analyses of cellular localisation, per-cell content and cell-cell  
648 interactions.

649

650 Finally, some of the original, pioneering, work in quantitative, flow cytometry-type  
651 immunofluorescence analysis of tissues (e.g., histocytometry (1-3,16,17)) relies upon commercial  
652 software for implementation, limiting accessibility. Moreover, whilst the histocytometry approach  
653 utilises both 2-D and 3-D confocal images, analyses have primarily focussed on the spatial  
654 relationships of just the CD-marker delineated cells. Our approach, supported by machine learning  
655 segmentation where necessary, enables precision analyses of *all* cells and hence highly accurate  
656 cell counting and per-cell quantifications within an entire section or region-of-interest.

657 Notwithstanding, here we focus on open-source, intestinal-specific 2-D delivery, as qualitative  
658 display in this format is today's gold standard, and because volumetric (*i.e.*, 3-D)  
659 immunofluorescence quantification is extremely challenging for routine usage, given the time  
660 requirements and increasing non-uniformities that manifest with imaging depth. With this in mind,  
661 the use of the confocal optical section provides 2-D immunofluorescence data that is *consistently*  
662 sampled, and thus well-suited for summation within cell-objects and for fair comparison across  
663 experimental samples. In turn, an important question for future work may involve addressing how far  
664 regular fluorescence images (*i.e.*, non-confocal) can be taken towards producing similar,  
665 quantitative results. To this end, herein we show how per-cell data can be extracted from FFPE



666 sections through the use of WGA staining to delineate cell outlines. This approach may prove  
667 important to success with regular fluorescence microscopy because FFPE sections can be cut  
668 much thinner than cryostat sections, and this physical section thickness itself may enable reliable  
669 extraction of per-cell information.

670

671 To conclude, here we have developed open, user-friendly methodology that delivers per-cell  
672 quantifications using routine, confocal microscopy-derived images of diverse gastrointestinal  
673 tissues. In combination, the presented approaches take the field of gastroenterology far beyond the  
674 representative image, and should now help to combat some of the data reproducibility issues that  
675 are associated with antibody technologies and over-reliance on qualitative tissue microscopy  
676 (36,37).

677

678

679 **Conflict of Interests Statement:**

680 The authors declare no conflicts of interest.

681

682 **Acknowledgements:**

683 The authors would like to acknowledge the UK Medical Research Council (grant number  
684 MR/R005699/1), the UK Engineering and Physical Sciences Research Council (grant  
685 EP/H008683/1) and the UK Biotechnology and Biological Sciences Research Council (grant number  
686 BB/P026818/1) for supporting the work. JWW is extremely grateful to Girton College and the  
687 University of Cambridge Herchel-Smith Fund for supporting him with Fellowships.

688

689

690

691

692

693

694 **BIBLIOGRAPHY**

695

696 1. Ecker RC, Steiner GE. Microscopy-based multicolor tissue cytometry at the single-cell level.  
697 Cytometry A 2004;59:182-90.

698

699 2. Harnett MM. Laser scanning cytometry: understanding the immune system in situ. Nat Rev  
700 Immunol 2007;7:897-904.

701

702 3. Gerner MY, Kastenmuller W, Ifrim I, Kabat J, Germain RN. Histo-cytometry: a method for  
703 highly multiplex quantitative tissue imaging analysis applied to dendritic cell subset  
704 microanatomy in lymph nodes. Proc Natl Acad Sci U S A 2012;37:364-76.

705

706 4. Bankhead P, Loughrey MB, Fernandez JA, Dombrowski Y, McArt DG, Dunne PD. QuPath:  
707 Open source software for digital pathology image analysis. Sci Rep 2017;7:16878.

708

709 5. McQuaid S, Gray RT, Murray LJ, Coleman HG, James JA, Salto-Tellez M, Hamilton PW,  
710 Blom S. Systems pathology by multiplexed immunohistochemistry and whole-slide digital  
711 image analysis. Sci Rep 2017;7:15580.

712

713 6. Schapiro D, Jackson HW, Raghuraman S. histoCAT: analysis of cell phenotypes and  
714 interactions in multiplex image cytometry data. Nat Methods 2017;14:873-876.

715

716 7. Morita N, Umemoto E, Fujita S, Hayashi A, Kikuta J, Kimura I, Haneda T, Imai T, Inoue A,  
717 Mimuro H and others. GPR31-dependent dendrite protrusion of intestinal CX3CR1(+) cells  
718 by bacterial metabolites. Nature 2019;566:110-114.

719

- 720 8. Moor AE, Harnik Y, Ben-Moshe S, Massasa EE, Rozenberg M, Eilam R, Bahar Halpern K,  
721 Itzkovitz S. Spatial Reconstruction of Single Enterocytes Uncovers Broad Zonation along the  
722 Intestinal Villus Axis. *Cell* 2018;175:1156-1167.e15.  
723
- 724 9. Eisenhoffer GT, Loftus PD, Yoshigi M, Otsuna H, Chien CB, Morcos PA, Rosenblatt J.  
725 Crowding induces live cell extrusion to maintain homeostatic cell numbers in epithelia.  
726 *Nature* 2012;484:546-9.  
727
- 728 10. Da Silva C, Wagner C, Bonnardel J, Gorvel JP, Lelouard H. The Peyer's Patch Mononuclear  
729 Phagocyte System at Steady State and during Infection. *Front Immunol* 2017;8:1254.  
730
- 731 11. Cummings RJ, Barbet G, Bongers G, Hartmann BM, Gettler K, Muniz L, Furtado GC, Cho J,  
732 Lira SA, Blander JM. Different tissue phagocytes sample apoptotic cells to direct distinct  
733 homeostasis programs. *Nature* 2016;539:565-569.  
734
- 735 12. Robertson D, Savage K, Reis-Filho JS, Isacke CM. Multiple immunofluorescence labelling of  
736 formalin-fixed paraffin-embedded (FFPE) tissue. *BMC Cell Biol* 2008;9:13.  
737
- 738 13. Weigert M, Schmidt U, Boothe T, Müller A, Dibrov A, Jain A, Wilhelm B, Schmidt D,  
739 Broaddus C, Culley S and others. Content-aware image restoration: pushing the limits of  
740 fluorescence microscopy. *Nat Methods* 2018;15:1090-1097.  
741
- 742 14. Carpenter AE, Kametsky L, Eliceiri KW. A call for bioimaging software usability. *Nat*  
743 *Methods* 2012;9:666-70.  
744
- 745 15. Carpenter AE, Jones TR, Lamprecht MR, Clarke C, Kang IH, Friman O, Guertin DA, Chang  
746 JH, Lindquist RA, Moffat J and others. CellProfiler: image analysis software for identifying  
747 and quantifying cell phenotypes. *Genome Biol* 2006;7:R100.

748

749 16. Li W, Germain RN, Gerner MY. Multiplex, quantitative cellular analysis in large tissue  
750 volumes with clearing-enhanced 3D microscopy (Ce3D). Proc Natl Acad Sci U S A  
751 2017;114:E7321-e7330.

752

753 17. Kotov DI, Pengo T, Mitchell JS, Gastinger MJ, Jenkins MK. Chrysalis: A New Method for  
754 High-Throughput Histo-Cytometry Analysis of Images and Movies. J Immunol 2019;202:300-  
755 308.

756

757 18. Schuffler PJ, Schapiro D, Giesen C, Wang HA, Bodenmiller B, Buhmann JM. Automatic  
758 single cell segmentation on highly multiplexed tissue images. Cytometry A 2015;87:936-42.

759

760 19. Caicedo JC, Cooper S, Heigwer F, Warchal S, Qiu P, Molnar C, Vasilevich AS, Barry JD,  
761 Bansal HS, Kraus O and others. Data-analysis strategies for image-based cell profiling. Nat  
762 Methods 2017;14:849.

763

764 20. Keita AV, Gullberg E, Ericson AC, Salim SY, Wallon C, Kald A, Artursson P, Soderholm JD.  
765 Characterization of antigen and bacterial transport in the follicle-associated epithelium of  
766 human ileum. Lab Invest 2006;86:504-16.

767

768 21. Moussata D, Goetz M, Gloeckner A, Kerner M, Campbell B, Hoffman A, Biesterfeld S,  
769 Flourie B, Saurin JC, Galle PR and others. Confocal laser endomicroscopy is a new imaging  
770 modality for recognition of intramucosal bacteria in inflammatory bowel disease in vivo. Gut  
771 2011;60:26-33.

772

773 22. kwikteam / npy-matlab: code to read and write NumPy's NPY format in MATLAB. GitHub  
774 repository. Available at <https://github.com/kwikteam/npy-matlab> Accessed March 25th, 2020.

775

776

777 23. Sommer C, Straehle C, Köthe U, Hamprecht FA. Ilastik: Interactive learning and  
778 segmentation toolkit. 2011 IEEE International Symposium on Biomedical Imaging: From  
779 Nano to Macro 2011:230-3.

780

781 24. Maska M, Ulman V, Svoboda D, Matula P, Matula P, Ederra C, Urbiola A, Espana T,  
782 Venkatesan S, Balak DM and others. A benchmark for comparison of cell tracking  
783 algorithms. *Bioinformatics* 2014;30:1609-17.

784

785 25. Everingham M, Van Gool L, Williams CKI, Winn J, Zisserman A. The Pascal Visual Object  
786 Classes (VOC) Challenge. *Int J Comput* 2010;88:303-338.

787

788 26. Falk T, Mai D, Bensch R, Çiçek Ö, Abdulkadir A, Marrakchi Y, Böhm A, Deubner J, Jäckel Z,  
789 Seiwald K and others. U-Net: deep learning for cell counting, detection, and morphometry.  
790 *Nat Methods* 2019;16:67-70.

791

792 27. Eilers PHC, Goeman JJ. Enhancing scatterplots with smoothed densities. *Bioinformatics*  
793 2004;20:623-628.

794

795 28. Ord JK, Getis A. Local Spatial Autocorrelation Statistics: Distributional Issues and an  
796 Application. *Geographical Analysis* 1995;27:286-306.

797

798 29. Dobbins WO, 3rd. Human intestinal intraepithelial lymphocytes. *Gut* 1986;27:972-85.

799

800 30. Pellegrino S, Villanacci V, Sansotta N, Scarfi R, Bassotti G, Vieni G, Princiotta A, Sferlazzas  
801 C, Magazzu G, Tuccari G. Redefining the intraepithelial lymphocytes threshold to diagnose  
802 gluten sensitivity in patients with architecturally normal duodenal histology. *Aliment*  
803 *Pharmacol Ther* 2011;33:697-706.

804

805 31. Rostami K, Marsh MN, Johnson MW, Mohaghegh H, Heal C, Holmes G, Ensari A, Aldulaimi  
806 D, Bancel B, Bassotti G and others. ROC-king onwards: intraepithelial lymphocyte counts,  
807 distribution & role in coeliac disease mucosal interpretation. *Gut* 2017;66:2080-2086.

808

809 32. De Jesus M, Ahlawat S, Mantis NJ. Isolating and immunostaining lymphocytes and dendritic  
810 cells from murine Peyer's patches. *J Vis Exp* 2013:e50167.

811

812 33. Reboldi A, Arnon TI, Rodda LB, Atakilit A, Sheppard D, Cyster JG. IgA production requires B  
813 cell interaction with subepithelial dendritic cells in Peyer's patches. *Science*  
814 2016;352:aaf4822.

815

816 34. Valle A, Barbagiovanni G, Jofra T, Stabilini A, Perol L, Baeyens A, Anand S, Cagnard N,  
817 Gagliani N, Piaggio E and others. Heterogeneous CD3 expression levels in differing T cell  
818 subsets correlate with the in vivo anti-CD3-mediated T cell modulation. *J Immunol*  
819 2015;194:2117-27.

820

821 35. Kreshuk A. Automating image analysis with machine learning. *Microscience Microscopy*  
822 *Congress*. Manchester, UK; 2019.

823

824 36. Uhlen M, Bandrowski A, Carr S, Edwards A, Ellenberg J, Lundberg E, Rimm DL, Rodriguez  
825 H, Hiltke T, Snyder M and others. A proposal for validation of antibodies. *Nat Methods*  
826 2016;13:823-827.

827

828 37. Baker M. Reproducibility crisis: Blame it on the antibodies. *Nature* 2015;521:274-6.

829

830

831

832 **FIGURE LEGENDS**

833 **Figure 1 - Open-source cell segmentation strategies for diverse intestinal tissues. A-D,**

834 Mouse villus mucosa frozen section. Here, we used a simple watershed approach that first defines  
835 the nucleus (gold, Hoechst 33342) of each cell, and then uses this as an anchor point from which to  
836 find each cell's actin-delineated boundary (grey, actin-AF633). **E-H**, Human Peyer's patch lymphoid  
837 tissue; formalin fixed paraffin embedded (FFPE) section. Exposure to alcohol during the FFPE  
838 process destroys the actin microfilaments (see **Figure S3**) so, instead, cell membranes were  
839 labelled using wheat germ agglutinin (WGA-AF633, blue). Watershed algorithms perform poorly in  
840 such densely-packed tissue types (shown, **Figure S4**), and so machine learning via the Ilastik  
841 software was instead used to produce probability maps of the cell outlines to enable segmentation  
842 (training shown in **E**, inset / process fully described, **Figure S2**). **I- L**, Rat mesenteric lymph node  
843 frozen section. Despite lower magnification and image resolution, the same machine learning  
844 based, Ilastik-CellProfiler process enables accurate cell segmentation. **B/F/J** - insets, Density  
845 plotting each cell's nuclear and cell outline fluorescence provides a straightforward approach to  
846 'gate out' incorrectly segmented cell objects with abnormally high (e.g., doublets) or low (e.g.,  
847 debris) signals. Example discarded events that lie outside of the indicated 'single-cell population'  
848 are indicated with gray squares on the tissue images. For all examples, segmentation accuracy  
849 scores are provided in **Figure S5**. Scale bars = 20 microns.

850

851 **Figure 2 - Conquering the representative image: *E. coli* passage into human control or IBD**

852 **ileal mucosa. A-C**, Mucosal tissue samples from the distal ileum of either a non-IBD cancer control  
853 patient (**B**) or an IBD patient (Crohn's disease) (**A** and **C**) were maintained *ex-vivo* in Ussing  
854 chambers. The apical sides of the living tissues were exposed to either Krebs buffer (**A**) or GFP-  
855 expressing, adherent invasive *E. coli* strain LF82 (**B/C**) for 20 minutes. Images of the mucosa were  
856 then collected randomly across 6-8 frozen sections per tissue sample prior to per-cell analysis for  
857 anti-GFP fluorescence to identify LF82. **D/E**, Instead of relying on representative images, the image-  
858 based cell profiling approach allowed quantification and display of *all* of the collected data (> 35,000

859 cells analysed in total). **D**, Concordance between the tissue samples taken per patient was  
860 observed (filled circles). Whilst the fluorescence distributions (lines represent averages) from the  
861 non IBD cancer control samples directly overlaid the Krebs buffer negative control (dashed line)  
862 suggesting no transmucosal uptake, the samples from the IBD patient all showed elevated  
863 fluorescence. **E**, Comparison between non-IBD and IBD groups for gated cells (indicated, **D**) with  
864 anti-GFP values greater than present in Krebs buffer control. (\*\*\*) Indicates statistical significance at  
865  $p < 0.001$  (Wilcoxon rank sum). Scale bars: **A-C** = 10  $\mu\text{m}$ .

866

867 **Figure 3 - Identifying intraepithelial T lymphocytes in large tilescans using a single CD**  
868 **marker.** Rat jejunal longitudinal tissue section. **A**, First, anti-epithelial cell adhesion molecule  
869 (EPCAM) immunofluorescence labelling was used to delineate the epithelium (*i.e.*, cells lying  
870 between the basement membrane and the apical enterocyte surface). **B**, As the anti-EPCAM  
871 antibody was raised in the same host species as the desired lymphocyte marker, the epithelium,  
872 lamina propria and lumen 'compartments' were directly-detected from the actin channel using pixel-  
873 classification machine learning in Ilastik (process outlined in **Figure S6**). **C**, A 112-image confocal  
874 tilescan labelled for nuclei, actin and anti-CD3 was collected. Each individual field was segmented  
875 into individual cells, and a software function was developed to spatially reassemble the images,  
876 segmentation masks and cell positions (> 60,000 cells). **D**, A region-of-interest (ROI) was placed  
877 around the tissue region containing optimally cross-sectioned villi, and the Ilastik model was used to  
878 predict and mask the epithelium (Pink). **D** - inset, CD3<sup>+</sup> cells inside or outside of this epithelial mask  
879 were then identified by gating against the secondary-only and isotype control per-cell fluorescence  
880 distributions (*i.e.*, as is typical in flow cytometry). Cell centroid markers were placed on each positive  
881 event. This approach permitted sensitive and accurate pinpointing of CD3<sup>+</sup> lymphocytes (**C**, inset).  
882 Scale bars: **A/B** = 25  $\mu\text{m}$ ; **C** = 50  $\mu\text{m}$ ; **D** = 1 mm.

883

884 **Figure 4 - Defining and counting T lymphocyte subpopulations on the basis of spatial**



885 **location.** Rat jejunum, continued from **Figure 3. A**, To differentiate intraepithelial (IEL) CD3<sup>+</sup> cells  
886 in close association with the apical side of the epithelium (*i.e.*, 'IEL<sup>sub</sup>') versus those *truly* in  
887 between enterocytes (*i.e.*, 'IEL<sup>inter</sup>'), the epithelial mask defined in **Figure 3** was skeletonised and  
888 dilated to form a central path enabling detection of IEL<sup>inter</sup> cells in each 'loop' of epithelium (method  
889 shown, **Figure S6**). **B/C**, The CD3<sup>+</sup> cell population was then split into three subpopulations: lamina  
890 propria CD3<sup>+</sup> (LP<sup>CD3+</sup>), IEL<sup>sub</sup> or IEL<sup>inter</sup>, and locations were displayed by marker placement on  
891 each cell's centroid. **D/E**, Typical examples of IEL<sup>sub</sup> and IEL<sup>inter</sup> events. **F**, Area measurements  
892 for the different tissue compartments. **G**, Total cell counts according to tissue compartment. **H**,  
893 Tissue compartment cell counts per 100 cells. **I**, Cell counts expressed as ratios between the  
894 different tissue compartments. Scale bars: **A/C** = 100 μm; **B** = 500 μm; **D/E** = 5 μm.

895

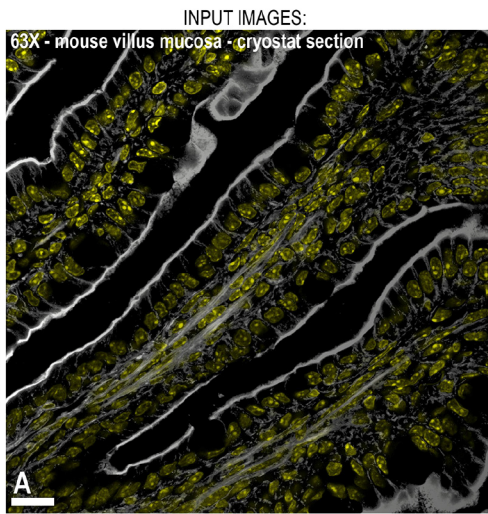
896 **Figure 5 - CD11c and CD3 expression in Peyer's patches.** Mouse ileal transverse section. **A**,  
897 The section was imaged as a 24- image tilescan labelled for nuclei, actin, anti-CD11c and anti-CD3.  
898 Transmitted and reflected light were also collected. **B**, The densely packed, lymphoid tissue  
899 segmented accurately into cells (~ 16,000) using the Ilastik/CellProfiler machine learning approach,  
900 and the software reassembly function spatially reassembled the data without artifacts at the overlap  
901 boundaries between the tiled images. **C/D**, The complexity of multichannel image (**A**) is dramatically  
902 reduced, using an example region-of-interest (yellow), and displaying the immunofluorescence  
903 markers (cyan = CD11c, magenta = CD3) on the segmented-cell outlines. **E/F**, CD3<sup>+</sup> and CD11c<sup>+</sup>  
904 cell populations were gated against secondary-only, leave-one-out and isotype control per-cell  
905 fluorescence distributions. In the densely packed tissue, a second sequential gate on fluorescence  
906 area per cell-object helped to reduce 'bystander-positive' events caused by fluorescence overlap  
907 into neighbouring cells (shown, **F** – inset) (further discussion/exemplification provided, **Figure S8**).  
908 **F**, Marker placement on the cell populations identified by the gating strategy in (**E**). Highly  
909 juxtaposed, and thus indicative of communication, CD11c-CD3 neighbouring cells (*i.e.*, region  
910 shown in **D**) that consequentially identified positive in *both* gates are shown with white markers.

911 Scale bars: **A/C/F** = 500  $\mu\text{m}$ ; **B** = 250  $\mu\text{m}$ ; **D** = 50  $\mu\text{m}$ .

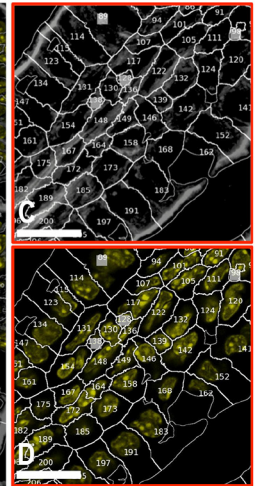
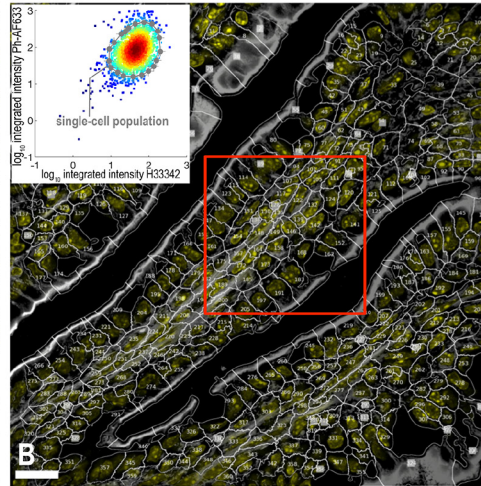
912

913 **Figure 6 - Mapping CD11c<sup>+</sup> and CD3<sup>+</sup> cell interactions, expression and spatial**  
914 **congregations.** Mouse ileum, continued from Figure 5. **A**, Cell-marker placement on the basis of  
915 immunofluorescence labelling. Highly juxtaposed CD11c-CD3 neighbouring cells that  
916 consequentially identified positive for both markers are shown with white markers. **B**, Flood-filling  
917 segmented cell objects provides a visually intuitive version of the data shown in (**A**) that can be  
918 displayed at a much smaller size. **C**, Here, the view shown in (**B**) is simplified to only show CD11c  
919 cells with touching CD3 nearest-cell neighbours, or juxtaposed cells that identify positive for both  
920 markers due to close spatial association. **D/E**, CD11c and CD3 expression maps with cell-objects  
921 coloured in four levels (*i.e.*, dim, lo, intermediate (int), hi) according to each segmented cell's level of  
922 immunofluorescence. **F**. Getis-Ord statistical map: this shows – as a probability heat map – where  
923 statistically significant congregations of cells are found relative to what would be expected by  
924 random chance given the frequencies of the different cell types. Scale bars: **A-F** = 500  $\mu\text{m}$ .

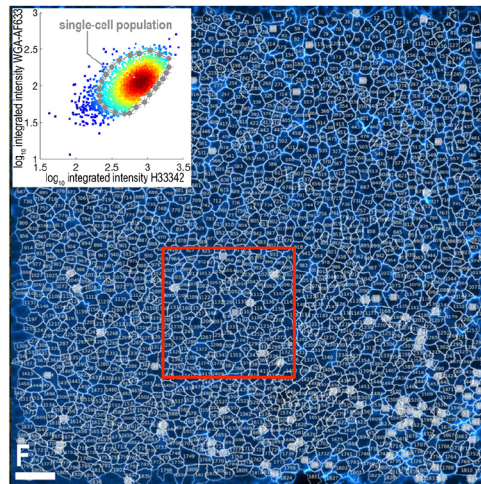
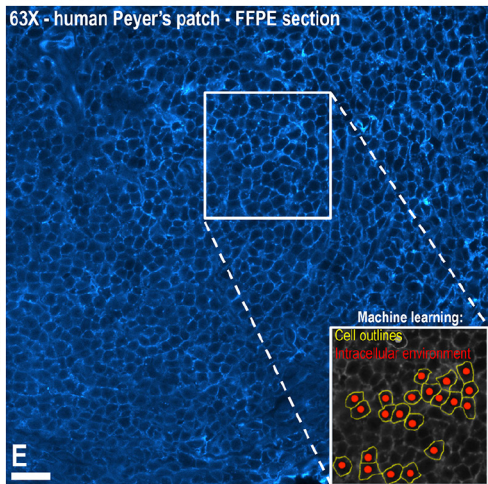
Phalloidin-AF633 / Hoechst 33342



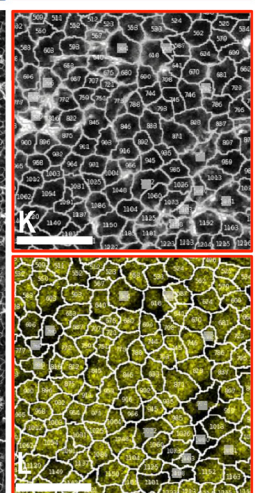
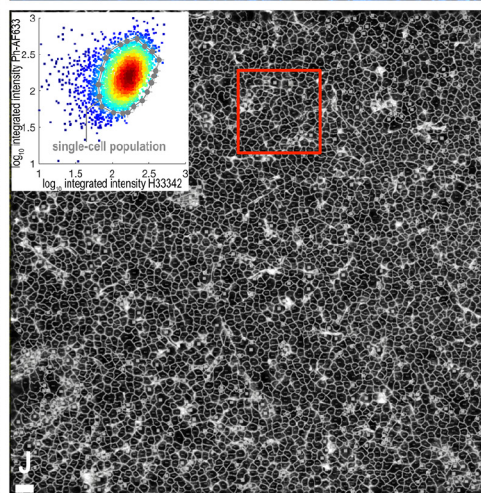
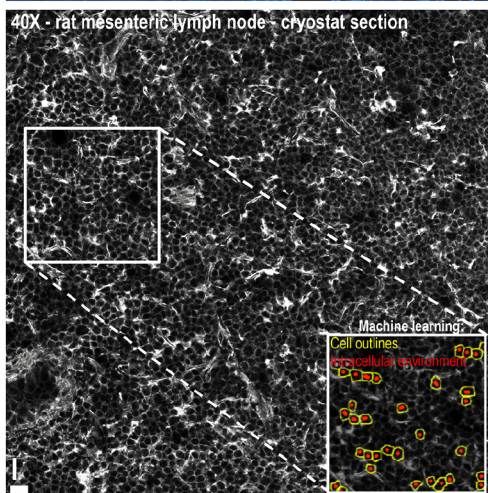
SEGMENTED CELLS / ■ DISCARDED EVENTS



WGA-AF633 / Hoechst 33342

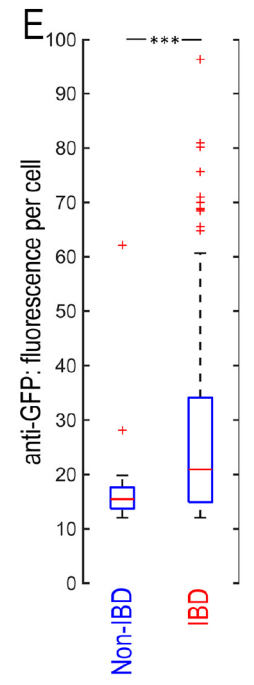
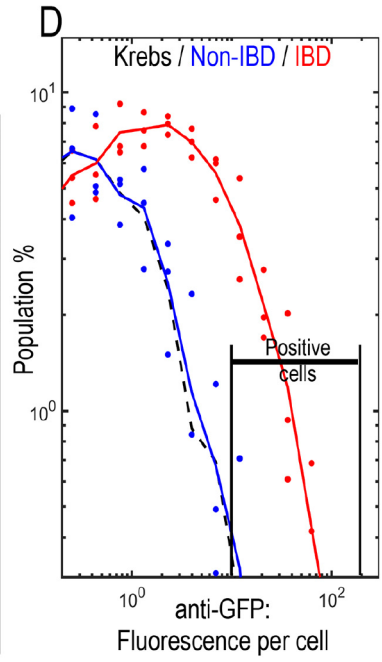
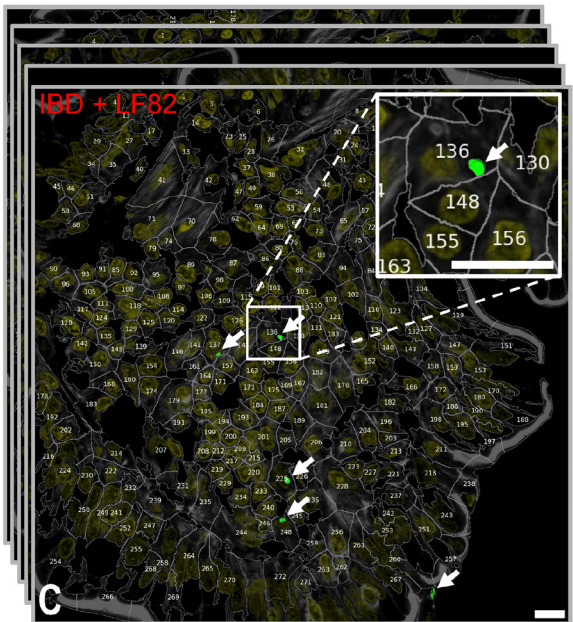
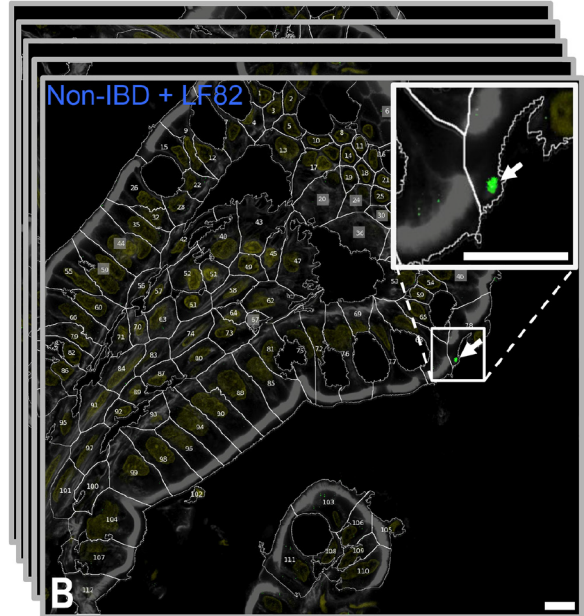
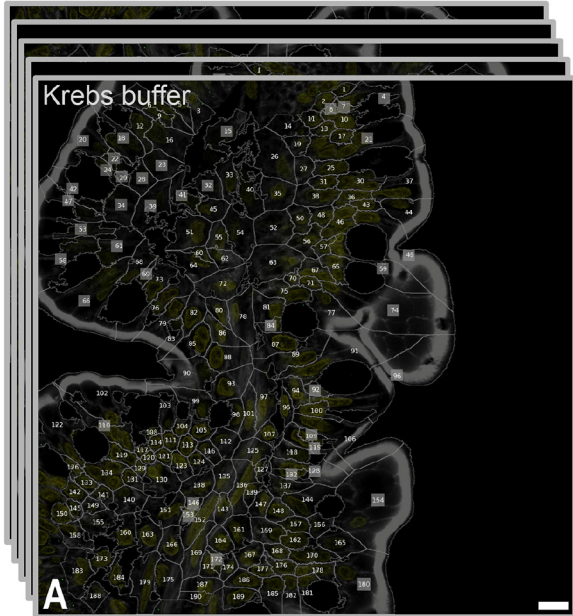


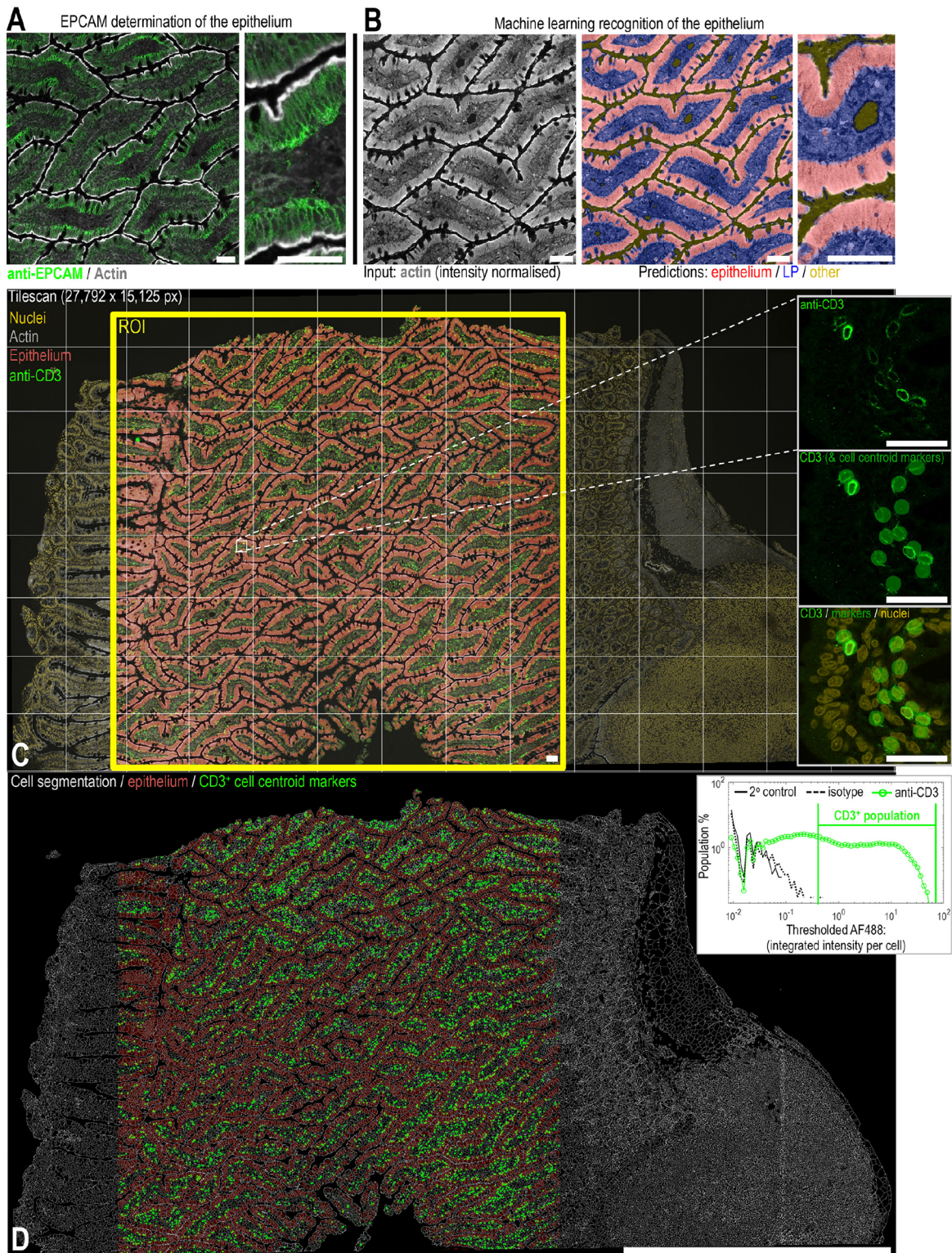
Phalloidin-AF633 / Hoechst 33342

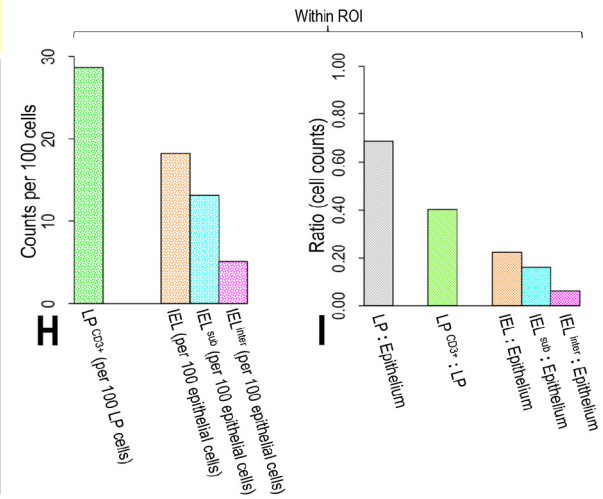
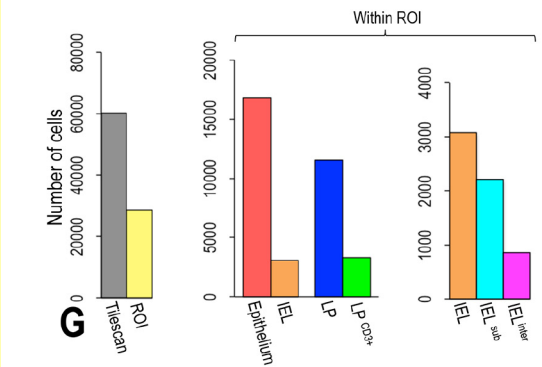
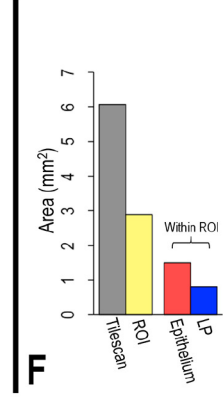
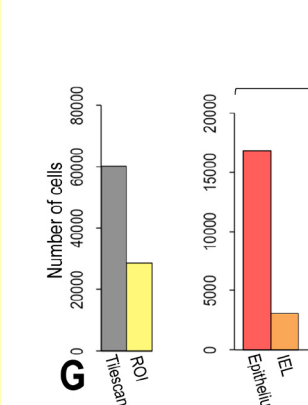
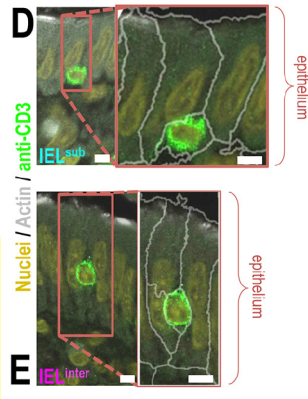
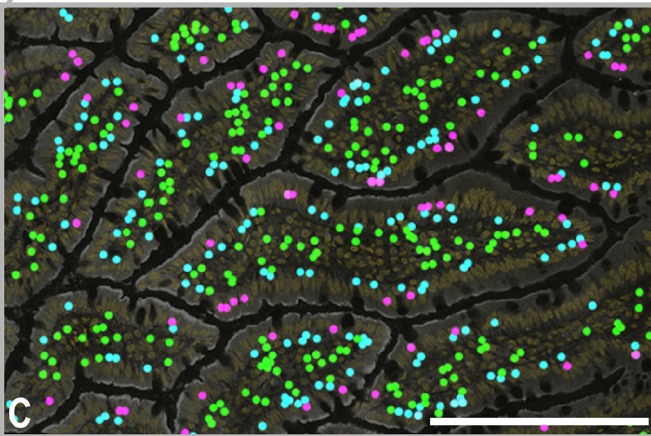
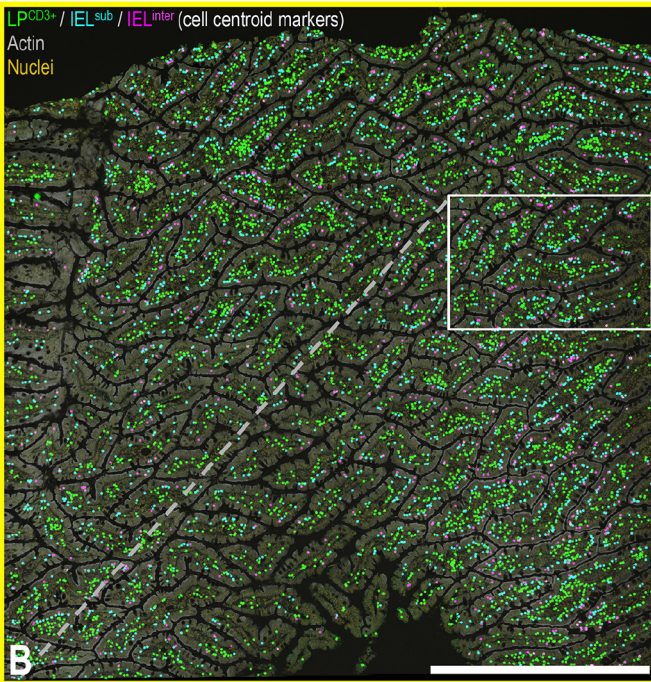
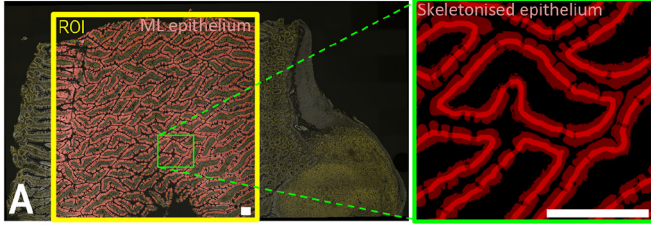


INPUT IMAGES:

Nuclei / Actin / anti-GFP







Tilescan (11,253 x 7,607 px)

Nuclei / Actin / anti-CD11c / anti-CD3 / brightfield / darkfield (scatter)

